

Thickness dependent transition from $1T'$ to Weyl semimetal phase in ultrathin MoTe_2 : Electrical transport, Noise and Raman studies

Manabendra Kuri,^{*} Subhadip Das,^{*} D V S Muthu, Anindya Das,[†] and A.K Sood[‡]
Department of Physics, Indian Institute of Science, Bangalore 560012, India

Bulk $1T'$ - MoTe_2 shows a structural phase transition from $1T'$ to Weyl semimetallic (WSM) T_d phase at ~ 240 K. This phase transition and transport properties in the two phases have not been investigated on ultra-thin crystals. Here we report electrical transport, $1/f$ noise and Raman studies in ultra-thin $1T'$ - MoTe_2 (~ 5 to 16 nm thick) field-effect transistors (FETs) devices as a function of temperature. The electrical resistivities for thickness 16 nm and 11 nm show maxima at temperatures 208 K and 178 K, respectively, making a transition from semiconducting to semimetallic phase, hitherto not observed in bulk samples. Raman frequencies and linewidths for 11 nm thick crystal show change around 178 K, attributed to additional contribution to the phonon self-energy due to enhanced electron-phonon interaction in the WSM phase. Further, the resistivity at low-temperature shows an upturn below 20 K along with the maximum in the power spectral density of the low frequency $1/f$ noise. The latter rules out the metal-insulator transition (MIT) being responsible for the upturn of resistivity below 20 K. The low temperature resistivity follows $\rho \propto 1/T$, changing to $\rho \propto T$ with increasing temperature supports electron-electron interaction physics at electron-hole symmetric Weyl nodes below 20 K. These observations will pave the way to unravel the properties of WSM state in layered ultra-thin van der Waals materials.

I. INTRODUCTION

Semimetallic transition metal dichalcogenides (TMDs) have spurred tremendous interest in recent years due to their novel electronic properties and a wide range of potential applications [1]. These materials exhibit exciting phenomena like gate tunable superconductivity [2, 3], charge density waves [4] and anomalous quantum Hall effect [5]. It has been shown that the T_d phase of semimetallic TMDs belong to a class of type-II Weyl semimetals (WSM) [6–11]. A WSM consists of topologically protected linear bands, touching at points referred to as 'Weyl nodes', where the band dispersion is linear in all the three momentum directions [12–15]. Not only different phases but also tunability of electronic properties of semimetallic TMDs by varying the number of layers have shown thickness-dependent transition temperature of the charge density wave in $1T$ - TiSe_2 and $1T$ - VSe_2 [16, 17] as well as magnetic and topological transitions [18]. However, the thickness-dependent electrical transport properties of semimetallic TMDs have not been explored well.

In this context MoTe_2 is a quite promising TMD for the following reasons. MoTe_2 crystallizes in normally three stable phases : hexagonal (α or 2H phase), monoclinic (β or $1T'$) and orthorhombic (γ or T_d phase) [19]. The 2H and $1T'$ phases are semiconducting in nature with bandgap of 1.1 and 0.06eV respectively [20, 21], whereas the T_d phase is a type-II WSM [22]. Bulk $1T'$ - MoTe_2 undergoes a first order structural phase transition from monoclinic $1T'$ to orthorhombic T_d phase below \sim

240 K [22–24]. Recent Raman studies [25–27] as well as ARPES measurements [28–30] confirm the bulk T_d phase of MoTe_2 to be a type-II WSM [6, 7, 31]. Recent magneto-transport measurements [32] of a few layer $1T'$ - MoTe_2 confirm its gapless semimetallic behavior. However, the transition from $1T'$ to T_d phase and their electrical transport properties, governed by the predicted electron-electron interactions at the Weyl nodes [33] have not been investigated on ultra-thin MoTe_2 crystals.

In this work, we report temperature dependent resistivity measurements of few layer $1T'$ - MoTe_2 devices with thickness ranging from 5 to 16 nm. We observe a clear signature of $1T'$ to T_d phase transition in 11 nm and 16 nm thick nanocrystals with a transition temperature (T_c) of 178 K and 208 K, much less than the bulk transition temperature (240 K). For $T > T_c$, semiconducting behavior with $d\rho/dT < 0$ is seen which changes to $d\rho/dT > 0$ below T_c , signifying semimetallic behavior. Such resistivity change is not seen in $1T'$ - MoTe_2 with thickness of 7 nm and 5 nm, establishing the suppression of transition in crystals with thickness below a critical value. In addition for the 11 nm thick crystal, the resistivity increases below $T \sim 20$ K. In the low temperature regime ($T < 20$ K), the resistivity shows $1/T$ behavior, a clear signature of the WSM state as predicted theoretically [33]. This feature has not been reported in bulk [22] but seen in 6 nm thick $1T'$ - MoTe_2 [32] where the upturn at ~ 20 K has been attributed to MIT [32]. We have used $1/f$ noise spectroscopy as a function of temperature to look at this suggestion of MIT, as noise spectroscopy has been used recently in VO_2 to examine the MIT [34]. We further note that $1/f$ noise measurements have been utilized as a sensitive tool to probe structural phase transitions [35, 36], vortex flux dynamics near superconductor-normal phase transition [37] and electronic phase transition [38, 39]. We will show that our $1/f$ noise spectra do not agree with this conjecture

^{*} These authors contributed equally

[†] anindya@iisc.ac.in

[‡] asood@iisc.ac.in

and propose that it is related to electron-electron interaction physics in the WSM state arising from the current carrying electron-hole states at the Weyl nodes [33]. Furthermore, we have carried out Raman scattering experiment as a function of temperature on 11 nm thick MoTe₂ device and show that Raman mode frequencies and linewidth exhibit slope change at T_c which further supports the transition from 1T' to WSM T_d phase observed in our electrical transport measurements.

II. EXPERIMENTAL DETAILS

Thin nanocrystals (between 5 and 16 nm) of 1T'-MoTe₂ were obtained from mechanical exfoliation of bulk single crystals of 1T'-MoTe₂ onto a piranha cleaned Si/SiO₂ substrate with 285 nm SiO₂ [40] with immediate spin-coating with PMMA to prevent degradation [41]. Electrical contacts were patterned using electron beam lithography followed by thermal deposition of Cr/Au (5 nm/70 nm). The nanocrystals were characterized by atomic force microscopy (AFM) (see Fig. S1 of the supplemental material).

Resistivity measurements were carried out in a home built dip-stick cryostat with a vacuum $\sim 10^{-6}$ mbar [41]. Two probe resistance measurements were carried out in a standard lock-in technique, by applying a small ac signal and measuring the current through the lock-in amplifier. The resistance fluctuations were recorded using a NI USB 6210 DAQ card. The details of noise measurement techniques have been discussed extensively in our earlier work [42]. Raman spectra were recorded using confocal Raman spectrometer (LABRAM HR-800) system using excitation wavelength of 532 nm with low incident power (~ 0.5 mW). The sample temperature was controlled using a liquid nitrogen cooled cryostat (M/s Linkham Scientific Thms350v).

III. RESULTS AND DISCUSSION

A. Transport study

Fig. 1(a) shows the resistivity (ρ) as a function of temperature (T) for two devices with thickness of 11 nm and 16 nm. It clearly shows that the resistivity first increases with the decreasing temperature ($d\rho/dT < 0$) as expected for the 1T' semiconducting phase, till a critical temperature T_c of 178 K for 11 nm thick 1T'-MoTe₂. Below T_c , the resistivity decreases ($d\rho/dT > 0$) showing semimetallic behavior until $T \sim 20$ K. A similar trend was also observed for 16 nm thick crystal with $T_c \sim 208$ K, showing clearly that T_c is suppressed as nanocrystal thickness is reduced. Inset of Fig. 1(a) shows derivative of the resistivity with temperature to determine T_c . Our observations are in variance with the reports by He *et al.*, where they observe semimetallic behavior (i.e $d\rho/dT > 0$) from 280 K down to 150 K for all

sample of thickness 7, 50, 180 nm and 100 μm [27]. Secondly, we do not observe hysteretic behavior in resistivity for 11 nm nanocrystal as observed in bulk [22, 27] (see Fig. S2(a)). For $T > T_c$, the resistivity shows Arrhenius behavior with activation gap of ~ 4 meV. Notably for thin nanocrystals (~ 5 nm and 7 nm) shown in Fig. 1(b), the resistivity increases monotonically as the temperature is reduced without a change in $d\rho/dT$. These devices remains semiconducting in the measured temperature range where the resistivity follows Arrhenius equation with activation energy of ~ 3.5 and 3.3 meV for 5 and 7 nm nanocrystals respectively (Figs. S2(b) and (c)). Thus, only the nanocrystals with thickness ≥ 11 nm show a transition from 1T' to T_d (WSM) phase. Although we have performed our electrical measurement in two probe configuration, the linear current to voltage relation (see Fig. S2(d)) of our 5nm thick sample at gate voltages ranging from -20V to 20V, suggests negligible Schottky barrier in our device fabrication process. In Fig. 1(c), we have plotted the transition temperature with the inverse of nanocrystal thickness for our 11 and 16nm samples with the reported T_c of the bulk crystal[22–24].

A qualitative understanding of the downward shift of T_c is as follows[27, 43]: In the T_d phase, the Fermi energy lies above the out-of-plane hole bands (marked as ψ_1 and ψ_2 in Ref. 43). With decreasing thickness, the confinement energy shifts the hole bands to lower energy and hence favors the formation of T_d phase at a lower temperature as compared to bulk 1T'-MoTe₂ (See the Figs. 4(a) and (b) of Ref. 27). The reason that T_d phase is not seen up to 10 K for 5nm and 7nm thick nanocrystals is because of the effect of unintentional hole doping. Gate dependent conductivity measurement (Fig. S2(e)) shows that the 5nm sample has conduction minima around +19 V of gate voltage (indicated by vertical dotted line in Fig. S2(e)) and not 0 V. Therefore, it is evident that at $V_{bg}=0$ V, the device is unintentionally hole doped. The explanation for this unintentional doping is following. It has been reported that rapid thermal annealing of 2H-MoTe₂ by oxygen at 250 $^{\circ}$ C shows p-type doping due to formation of Mo-O bonds in tellurium vacancy sites [44]. Similar effect is also observed on this material for prolonged exposure in the atmosphere [45], which can also be expected for 1T'-MoTe₂. The effect of unintentional hole doping will be more in the thin samples due to relative increase in surface area and stabilize the 1T' phase [43]. Paul *et al.* [46] show that 2 to 5 layers of MoTe₂ are in 1T' phase at room temperature as indicated by the 130 cm^{-1} Raman mode [25–27]. By electron doping these samples using NH₃ exposure, the 130 cm^{-1} mode show splitting, indicative of the T_d phase [25–27]. More theory work is needed to quantitatively understand this effect.

We now discuss the low temperature resistivity (4-100 K) for the 11 nm nanocrystal (zoomed part of Fig. 1(a)) to focus on the resistivity minimum at ~ 20 K (Fig. 1(d)). Similar upturn in resistivity at temperatures below 10 K was observed in 6 nm 1T'-MoTe₂ crystal [32], which

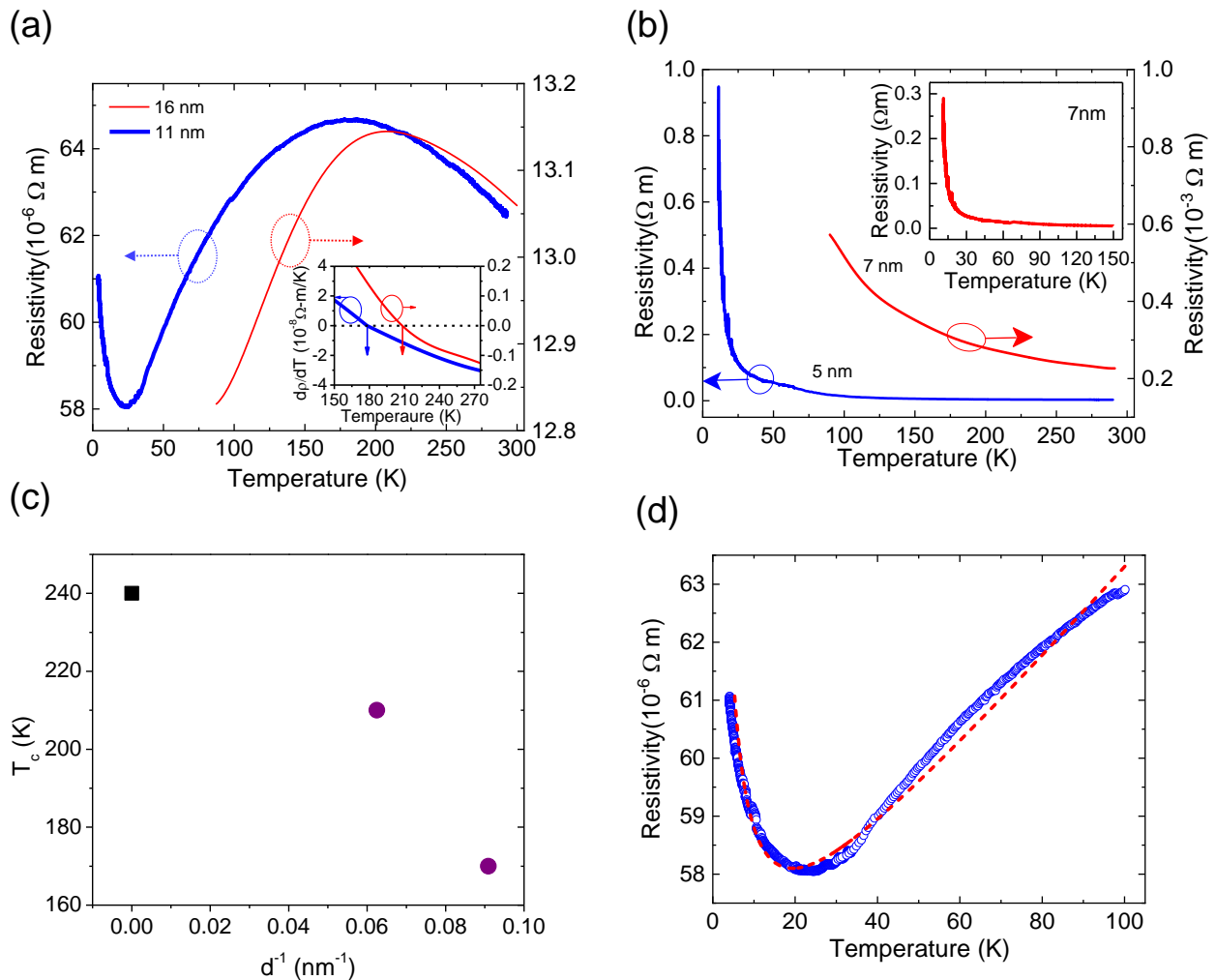


FIG. 1. (Color Online) (a) Resistivity (ρ) versus temperature (T) for ~ 11 nm and ~ 16 nm nanocrystals. Inset shows $d\rho/dT$ with temperature. T_c is indicated with vertical arrows. (b) Resistivity (ρ) versus temperature (T) for thin nanocrystals ~ 5 nm and ~ 7 nm respectively. Inset shows the resistivity data in the low temperature regime (10 to 150K) of another 7 nm thick device. (c) Critical temperature (T_c) as a function of inverse of nanocrystal thickness (d^{-1}) (circle points) from Fig. 1(a). The error bar size is ~ 0.5 K. The bulk $T_c \sim 240$ K (Square dot) has been taken from literature [22–24]. (d) Resistivity (ρ) versus temperature (T) in the low temperature regime (4 K to 100 K) for ~ 11 nm nanocrystal. The red dashed line shows the fit with Eq. (1).

was attributed to enhanced e-e interactions in two dimension where the resistivity $\rho \propto \log_{10}(T)$. For 3.6 nm nanocrystal, it was shown that the resistivity increases as the temperature is lowered from ambient to 1.5 K, which was attributed to strong localization effect [32]. It was argued that the lower value of the electron dephasing length (L_Φ) in ultrathin crystals leads to enhanced localization, resulting in MIT at low temperatures [32]. However, our low-temperature upturn resistivity data of 11 nm thick nanocrystal do not scale as $\log_{10}(T)$ or follow MIT scaling power law as observed in low frequency noise measurements [34]. We will come back to it when we discuss the noise measurements in the next section. Regarding the upturn of resistivity below 20 K, we note that the theoretically predicted resistivity in the WSM

state in the clean limit has electron-electron interactions with zero total momentum transfer due to electron-hole symmetry near the Weyl nodes that leads to $1/T$ dependence [33]. Guided by this, we fit our resistivity data with the equation

$$\rho = \rho_0 + \frac{a}{T} + bT \quad (1)$$

The third term on the right hand side, linear relation of ρ with T , is due to electron-phonon interactions, whose nature is determined by the Bloch-Grüneisen temperature (Θ_{BG}) rather than the Debye temperature (Θ_D) for smaller Fermi surfaces around the Weyl nodes as observed in graphene [47]. Fig. 1(d) shows the fit to Eq.(1), where we observe that for $T < 20$ K, $\rho \propto 1/T$ dominates and for $T > 20$ K, $\rho \propto T$. We note that addition

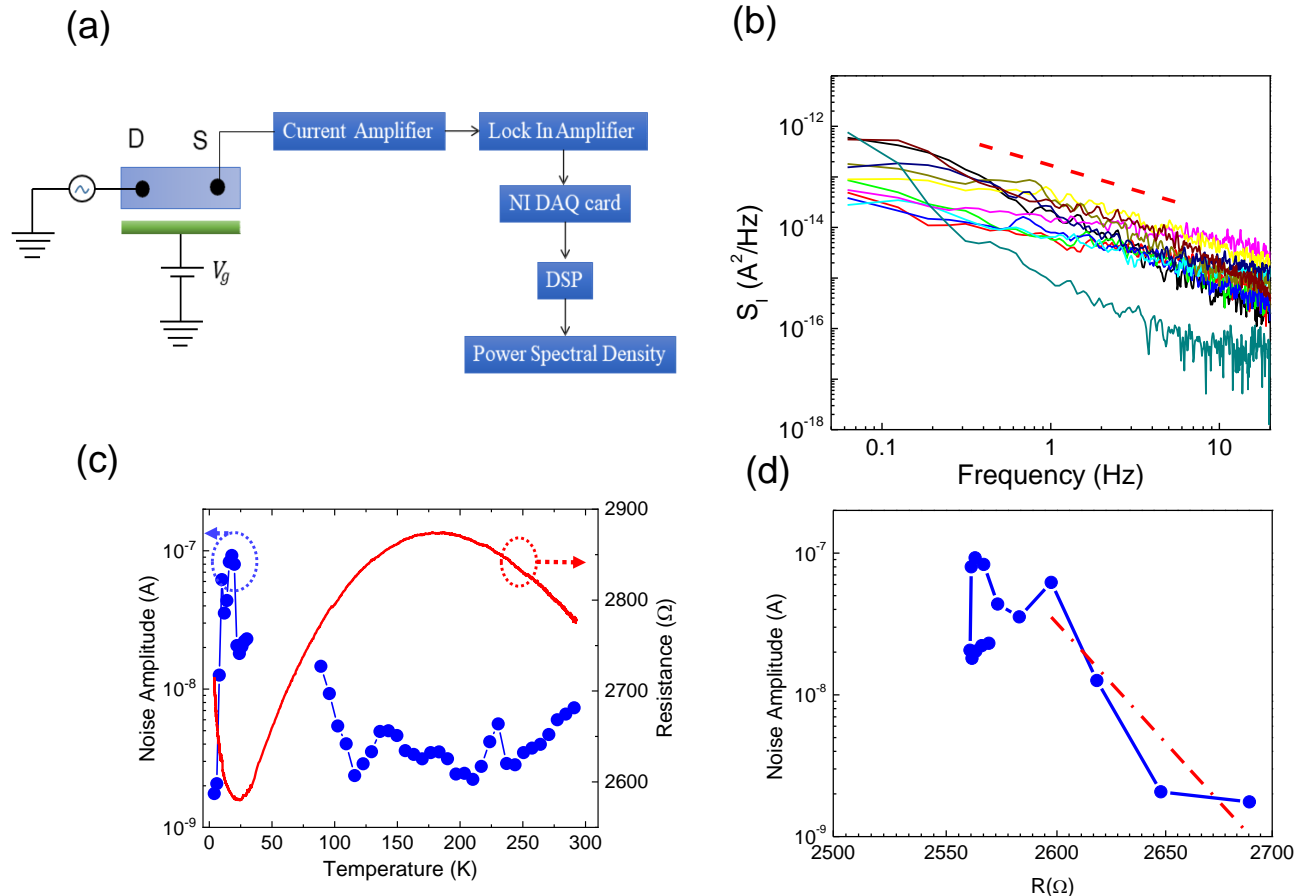


FIG. 2. (Color Online) (a) Schematic of $1/f$ noise measurement. (b) Power spectral density for several values of temperatures (T). (c) Noise amplitude (A) - blue solid symbols and resistance versus temperature - red line. (d) Noise scaling: Noise amplitude with resistance.

of a term in resistivity proportional to T^2 arising from electron-electron interaction in Fermi liquid does not fit the data.

B. Noise measurements

Fig. 2(a) shows the schematic of the $1/f$ noise measurements. Two probe voltage noise was measured using the technique described in our earlier work [42]. The linear current variation at low bias voltage (Fig. S2(d)) of our 5nm nanocrystal at 77K show negligible Schottky barrier at the interface of channel and electrode and hence rules out the possibility of any spurious contribution to noise measurements from the device contacts. Fig. 2(b) shows the typical power spectral density (PSD) for several temperatures where the dashed line shows the slope-1. The PSD in our case is $\sim 1/f^\beta$, where β lies between 0.8 to 1.2. Fig. 2(c) shows the comparison of the noise am-

plitude (A) and resistance with temperature. The noise amplitude A , changes by two orders of magnitude with temperature, with a maximum at $\sim 20K$. In Fig. 2(d), we re-plot the Noise amplitude versus resistance (R) to examine the expected scaling seen earlier near MIT [34]. The noise scaling close to MIT transition is $S_I/I^2 \propto R^x$, where x is the universal exponent [34]. For MIT, $x \sim 2.6$ [34]. In comparison, in our case $x \sim 100$ which is shown by the dotted line in Fig. 2(d). Thus the scaling of noise with resistance near 20K transition is not compatible with MIT. We hope that our experiments will motivate theoretical understanding of noise fluctuations in Weyl semimetals.

C. Raman spectroscopy

At ambient condition, $1T'$ -MoTe₂ belongs to $P2_1/m$ space group which gives 18 Raman active modes (12

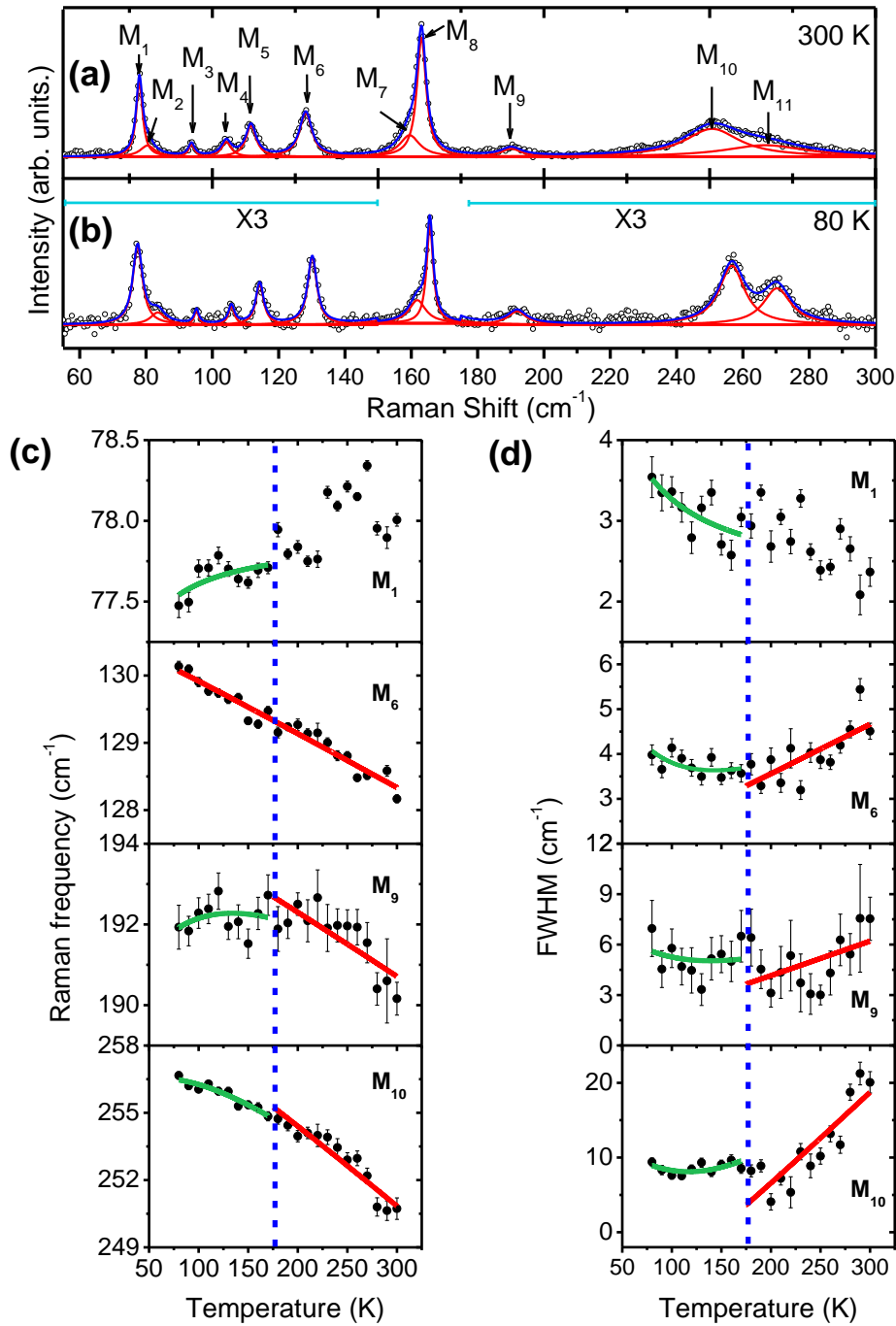


FIG. 3. (Color Online) Raman spectra of 11 nm thin nanocrystal at (a) 300 and (b) 80 K. Black circles represents experimentally captured data points. Solid lines (Blue and red) are their respective Lorentzian fit. The peaks are shown from M₁ to M₁₁. Some regions at low temperature phase have been enhanced (ranges shown by green lines) for low signal response. (c) Peak position and (d) full width half maxima plot with temperature of M₁, M₆, M₉ and M₁₀ modes. The cubic anharmonic fitting is represented by the red line. Green lines represents the fitting from linear combination of cubic anharmonic and EPC contribution. Blue dashed line indicates the transition temperature (T_c) from 1T' to WSM phase.

$A_g+6 B_g$) [48]. Fig. 3 shows Raman spectra of 11 nm thick MoTe₂ at 300 and 80 K, displaying 11 Raman modes, labeled as M₁ to M₁₁. Spectra are fitted with a sum of Lorentzian functions to extract phonon frequency (ω) and linewidth (γ) as a function of temperature, and

plotted in Figs. 3(c), 3(d) and Fig. S3. Recent report shows appearance of an additional weak Raman mode near ~ 130 cm⁻¹ in the bulk T_d phase below the transition temperature 240 K [25–27]. However our measurements on 11nm thick 1T'-MoTe₂ do not show this addi-

tional new Raman modes down to 80 K. Theoretical and experimental results by Ma *et al.* report that $1T'$ and T_d phases of MoTe_2 have similar Raman spectra with two A_g modes near $\sim 130 \text{ cm}^{-1}$ with a difference of only $\sim 1 \text{ cm}^{-1}$ [49]. It is very likely that this separation is not resolved in our 11nm thin crystal. At a first glance, the following observations are noteworthy in Figs. 3(c) and (d): (i) The frequency and linewidth of the mode M_1 show anomalous temperature dependence namely, the frequency decreases and linewidth increases with decreasing temperature. (ii) The linewidth of modes M_6 , M_9 and M_{10} tend to show either saturation or increase below T_c . (iii) The frequency of modes M_9 and M_{10} show marked deviation from linear dependence on temperature expected from cubic anharmonicity. To understand these trends, we recall that in a solid, a phonon can decay into two or more phonons (anharmonic contribution) or it can create a pair of electron and hole (electron-phonon coupling (EPC)) in conduction and valence bands respectively. These contribution to the phonon frequency and linewidth can be written as,

$$\omega(T) = \omega_0 + \Delta\omega_{ph} + \Delta\omega_{e-ph} \quad (2)$$

$$\gamma(T) = \gamma_0 + \Delta\gamma_{ph} + \Delta\gamma_{e-ph} \quad (3)$$

In a simplified model, taking cubic anharmonicity into account for the decay of a phonon into two phonons of equal energy, the temperature dependence is given by: $\Delta\omega_{ph}(T) = -A.g(T, \omega_0)$ and $\Delta\gamma_{ph}(T) = B.g(T, \omega_0)$, where $g(T, \omega_0) = 1 + 2/(e^{\hbar\omega_0/2k_B T} - 1)$ with ω_0 being the phonon frequency at zero temperature, and k_B is the Boltzmann constant [50], A and B are positive constants proportional to the phonon-phonon interaction strength. Neglecting the EPC contribution, the anharmonic decay model alone fails to capture the temperature dependence of ω for M_9 and M_{10} and γ for M_6 , M_9 and M_{10} modes below T_c (Figs. 3(c) and (d)). In addition, M_1 mode shows opposite temperature dependence of ω and γ from cubic anharmonicity. We now argue that these anomalous changes below T_c are due to strong EPC between Weyl Fermions and phonons in the WSM state.

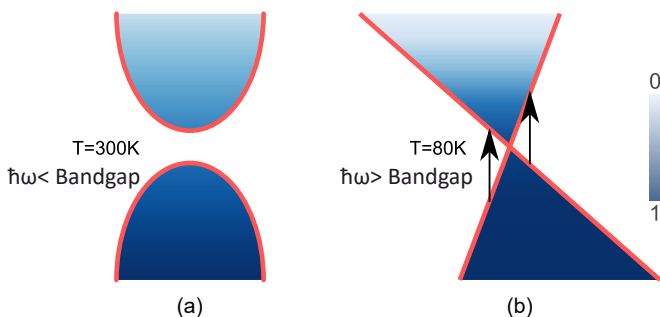


FIG. 4. Schematic illustration of the electronic bands in (a) $1T'$ and (b) WSM phase of MoTe_2 . The arrows in the WSM phase represents electronic transition. The blue gradient represents the color map of the Fermi-Dirac distribution at 80K and 300K respectively.

Fig. 4 shows a schematic of the electronic states near Fermi energy, above and below T_c . The self-energy of the phonons due to EPC arises from the interband transition at the energy of the phonon mode ($\hbar\omega_0$) as indicated by the arrows in Fig. 4. At $T > T_c$, the semiconducting $1T'$ phase has a bandgap of $\sim 60 \text{ meV}$ [21]. Since the bandgap is larger than the energies of the phonons, the electronic transitions at $\hbar\omega_0$ do not occur and hence the contribution from the EPC to the phonon self-energy can be neglected. At $T < T_c$ in the gapless WSM state (shown in Fig. 4), the electron-hole excitations at the phonon energy $\hbar\omega_0$ become feasible, resulting in considerable electron-phonon interaction. In the WSM state, real part of the self-energy due to EPC contribute to the additional softening of the phonon frequency and the imaginary part to the additional linewidth of the Raman mode [51]. Following Ref. 52, the EPC contribution to phonon linewidth is, $\Delta\gamma_{e-ph}(T) = D.h(T, \omega_0)$ where D is a positive constant and $h(T, \omega_0) = [f(-\frac{\hbar\omega_0}{2}) - f(\frac{\hbar\omega_0}{2})]$, with $f(x)$ representing the Fermi function. Assuming similar expression for the EPC contribution to the mode frequency, $\Delta\omega_{e-ph}(T)$ can be expressed as $-C.h(T, \omega_0)$ with positive constant C. Eqs. (2) and (3) are fitted to the data (green line) below T_c (Figs. 3(c) and(d)). Table. S1 shows the extracted parameters with error bars. As seen in Fig. 3, the inclusion of electron-phonon contribution, captures the anomalous temperature dependence of ω and γ below T_c , supporting the transition to WSM phase. However for the M_1 mode, ω slightly increases and γ slightly decreases (both by $\sim 0.5 \text{ cm}^{-1}$) even above T_c and cannot be explained by our model and requires further study (Fig. 3).

IV. CONCLUSION

In summary, we have carried out electrical transport measurements and Raman studies as a function of temperature in ultrathin $1T'$ - MoTe_2 . The nanocrystals with thickness larger than 11 nm show a resistance maximum which is attributed to a transition from $1T'$ to T_d (WSM) state on cooling. Furthermore, the resistivity increase at low temperatures for $T < 20K$ shows $\rho \propto 1/T$, a signature of the WSM state. This is further supported by our $1/f$ electrical-noise studies. Temperature induced transition from topologically trivial $1T'$ phase to type-II Weyl semimetallic T_d phase is also captured by means of anomalous temperature dependence of few phonon frequencies and their linewidths due to contribution from the electron-phonon coupling in the WSM phase. We hope that our studies will motivate theoretical studies to quantitatively understand the absence of the WSM in ultrathin $1T'$ - MoTe_2 due to possible gap opening at the Weyl point and the temperature dependence of the $1/f$ power spectral density.

ACKNOWLEDGEMENT

The authors would like to acknowledge the Center for Nanoscience and Engineering (CENSE), IISc for fabrica-

tion facilities. AD and AKS thank the Department of Science and Technology (DST) for funding with DSTO-2051 and Nanomission project as well as Year of Science Professorship.

-
- [1] Q. H. Wang, K. Kalantar-Zadeh, A. Kis, J. N. Coleman, and M. S. Strano, *Nature Nanotechnology* **7**, 699 (2012).
- [2] R. C. Morris, R. V. Coleman, and R. Bhandari, *Phys. Rev. B* **5**, 895 (1972).
- [3] E. Sajadi, T. Palomaki, Z. Fei, W. Zhao, P. Bement, C. Olsen, S. Luescher, X. Xu, J. A. Folk, and D. H. Cobden, *Science* **362**, 922 (2018).
- [4] D. E. Moncton, J. D. Axe, and F. J. DiSalvo, *Phys. Rev. B* **16**, 801 (1977).
- [5] K. Kang, T. Li, E. Sohn, J. Shan, and K. F. Mak, *Nature Materials* **18**, 324 (2019).
- [6] A. A. Soluyanov, D. Gresch, Z. Wang, Q. Wu, M. Troyer, X. Dai, and B. A. Bernevig, *Nature* **527**, 495 (2015).
- [7] Z. Wang, D. Gresch, A. A. Soluyanov, W. Xie, S. Kushwaha, X. Dai, M. Troyer, R. J. Cava, and B. A. Bernevig, *Phys. Rev. Lett.* **117**, 056805 (2016).
- [8] Y. Wang, E. Liu, H. Liu, Y. Pan, L. Zhang, J. Zeng, Y. Fu, M. Wang, K. Xu, Z. Huang, *et al.*, *Nature Communications* **7**, 13142 (2016).
- [9] X. Qian, J. Liu, L. Fu, and J. Li, *Science* **346**, 1344 (2014).
- [10] A. A. Zyuzin and A. A. Burkov, *Phys. Rev. B* **86**, 115133 (2012).
- [11] D. T. Son and B. Z. Spivak, *Phys. Rev. B* **88**, 104412 (2013).
- [12] S.-Y. Xu, I. Belopolski, D. S. Sanchez, C. Zhang, G. Chang, C. Guo, G. Bian, Z. Yuan, H. Lu, T.-R. Chang, *et al.*, *Science Advances* **1**, e1501092 (2015).
- [13] S.-Y. Xu, I. Belopolski, N. Alidoust, M. Neupane, G. Bian, C. Zhang, R. Sankar, G. Chang, Z. Yuan, C.-C. Lee, S.-M. Huang, H. Zheng, J. Ma, D. S. Sanchez, B. Wang, A. Bansil, F. Chou, P. P. Shibayev, H. Lin, S. Jia, and M. Z. Hasan, *Science* **349**, 613 (2015).
- [14] B. Lv, N. Xu, H. Weng, J. Ma, P. Richard, X. Huang, L. Zhao, G. Chen, C. Matt, F. Bisti, *et al.*, *Nature Physics* **11**, 724 (2015).
- [15] L. Yang, Z. Liu, Y. Sun, H. Peng, H. Yang, T. Zhang, B. Zhou, Y. Zhang, Y. Guo, M. Rahn, *et al.*, *Nature Physics* **11**, 728 (2015).
- [16] P. Goli, J. Khan, D. Wickramaratne, R. K. Lake, and A. A. Balandin, *Nano Letters* **12**, 5941 (2012).
- [17] J. Yang, W. Wang, Y. Liu, H. Du, W. Ning, G. Zheng, C. Jin, Y. Han, N. Wang, Z. Yang, *et al.*, *Appl. Phys. Lett.* **105**, 063109 (2014).
- [18] M. M. Otrokov, I. P. Rusinov, M. Blanco-Rey, M. Hoffmann, A. Y. Vyazovskaya, S. V. Eremin, A. Ernst, P. M. Echenique, A. Arnau, and E. V. Chulkov, *Phys. Rev. Lett.* **122**, 107202 (2019).
- [19] D. Puotinen and R. Newnham, *Acta Cryst.* **14**, 691 (1961).
- [20] C. Ruppert, O. B. Aslan, and T. F. Heinz, *Nano Lett.* **14**, 6231 (2014).
- [21] D. H. Keum, S. Cho, J. H. Kim, D.-H. Choe, H.-J. Sung, M. Kan, H. Kang, J.-Y. Hwang, S. W. Kim, H. Yang, *et al.*, *Nature Physics* **11**, 482 (2015).
- [22] Y. Qi, P. G. Naumov, M. N. Ali, C. R. Rajamathi, W. Schnelle, O. Barkalov, M. Hanfland, S.-C. Wu, C. Shekhar, Y. Sun, *et al.*, *Nature Communications* **7**, 11038 (2016).
- [23] R. Sankar, G. Narsinga Rao, I. P. Muthuselvam, C. Butler, N. Kumar, G. Senthil Murugan, C. Shekhar, T.-R. Chang, C.-Y. Wen, C.-W. Chen, W.-L. Lee, M.-T. Lin, H.-T. Jeng, C. Felser, and F. C. Chou, *Chemistry of Materials* **29**, 699 (2017).
- [24] R. Clarke, E. Marseglia, and H. Hughes, *Philosophical Magazine B* **38**, 121 (1978).
- [25] K. Zhang, C. Bao, Q. Gu, X. Ren, H. Zhang, K. Deng, Y. Wu, Y. Li, J. Feng, and S. Zhou, *Nature Communications* **7**, 13552 (2016).
- [26] S.-Y. Chen, T. Goldstein, D. Venkataraman, A. Ramasubramaniam, and J. Yan, *Nano Lett.* **16**, 5852 (2016).
- [27] R. He, S. Zhong, H. H. Kim, G. Ye, Z. Ye, L. Winford, D. McHaffie, I. Rilak, F. Chen, X. Luo, Y. Sun, and A. W. Tsien, *Phys. Rev. B* **97**, 041410 (2018).
- [28] L. Huang, T. M. McCormick, M. Ochi, Z. Zhao, M.-T. Suzuki, R. Arita, Y. Wu, D. Mou, H. Cao, J. Yan, *et al.*, *Nature Materials* **15**, 1155 (2016).
- [29] K. Deng, G. Wan, P. Deng, K. Zhang, S. Ding, E. Wang, M. Yan, H. Huang, H. Zhang, Z. Xu, *et al.*, *Nature Physics* **12**, 1105 (2016).
- [30] A. N. Berger, E. Andrade, A. Kerelsky, D. Edelberg, J. Li, Z. Wang, L. Zhang, J. Kim, N. Zaki, J. Avila, *et al.*, *npj Quantum Materials* **3**, 2 (2018).
- [31] Y. Sun, S.-C. Wu, M. N. Ali, C. Felser, and B. Yan, *Phys. Rev. B* **92**, 161107 (2015).
- [32] P. Song, C. Hsu, M. Zhao, X. Zhao, T.-R. Chang, J. Teng, H. Lin, and K. P. Loh, *2D Materials* **5**, 031010 (2018).
- [33] P. Hosur, S. A. Parameswaran, and A. Vishwanath, *Phys. Rev. Lett.* **108**, 046602 (2012).
- [34] Z. Topalian, S.-Y. Li, G. A. Niklasson, C. G. Granqvist, and L. B. Kish, *Journal of Applied Physics* **117**, 025303 (2015).
- [35] U. Chandni, A. Ghosh, H. S. Vijaya, and S. Mohan, *Phys. Rev. Lett.* **102**, 025701 (2009).
- [36] C. Barone, F. Lang, C. Mauro, G. Landi, J. Rappich, N. H. Nickel, B. Rech, S. Pagano, and H. C. Neitzert, *Scientific Reports* **6**, 34675 (2016).
- [37] D. Babić, J. Bentner, C. Sürgers, and C. Strunk, *Phys. Rev. B* **76**, 134515 (2007).
- [38] R. Koushik, M. Baenninger, V. Narayan, S. Mukerjee, M. Pepper, I. Farrer, D. A. Ritchie, and A. Ghosh, *Phys. Rev. B* **83**, 085302 (2011).
- [39] C. Barone, E. Bellingeri, M. Adamo, E. Sarnelli, C. Ferdeghini, and S. Pagano, *Superconductor Science and Technology* **26**, 075006 (2013).
- [40] M. Kuirri, B. Chakraborty, A. Paul, S. Das, A. Sood, and A. Das, *Appl. Phys. Lett.* **108**, 063506 (2016).
- [41] M. Kuirri, C. Kumar, B. Chakraborty, S. N. Gupta, M. H. Naik, M. Jain, A. Sood, and A. Das, *Nanotechnology* **26**, 485704 (2015).

- [42] C. Kumar, M. Kuri, J. Jung, T. Das, and A. Das, *Nano Letters* **16**, 1042 (2016).
- [43] H.-J. Kim, S.-H. Kang, I. Hamada, and Y.-W. Son, *Phys. Rev. B* **95**, 180101 (2017).
- [44] D. Qu, X. Liu, M. Huang, C. Lee, F. Ahmed, H. Kim, R. S. Ruoff, J. Hone, and W. J. Yoo, *Advanced Materials* **29**, 1606433.
- [45] N. Haratipour and S. J. Koester, in *72nd Device Research Conference* (2014) pp. 171–172.
- [46] S. Paul, S. Karak, M. Mandal, A. Ram, S. Marik, R. Singh, and S. Saha, *arXiv preprint arXiv:1910.09996* (2019).
- [47] D. K. Efetov and P. Kim, *Phys. Rev. Lett.* **105**, 256805 (2010).
- [48] B. E. Brown, *Acta Crystallographica* **20**, 268 (1966).
- [49] X. Ma, P. Guo, C. Yi, Q. Yu, A. Zhang, J. Ji, Y. Tian, F. Jin, Y. Wang, K. Liu, T. Xia, Y. Shi, and Q. Zhang, *Phys. Rev. B* **94**, 214105 (2016).
- [50] M. Balkanski, R. F. Wallis, and E. Haro, *Phys. Rev. B* **28**, 1928 (1983).
- [51] J. Menéndez and M. Cardona, *Phys. Rev. B* **29**, 2051 (1984).
- [52] B. Xu, Y. M. Dai, L. X. Zhao, K. Wang, R. Yang, W. Zhang, J. Y. Liu, H. Xiao, G. Chen, S. A. Trugman, *et al.*, *Nature Communications* **8**, 14933 (2017).

Supplemental Material

Manabendra Kuiri,* Subhadip Das,* D V S Muthu, Anindya Das,[†] and A.K Sood[‡]
Department of Physics, Indian Institute of Science, Bangalore 560012, India

I. DEVICE CHARACTERIZATION

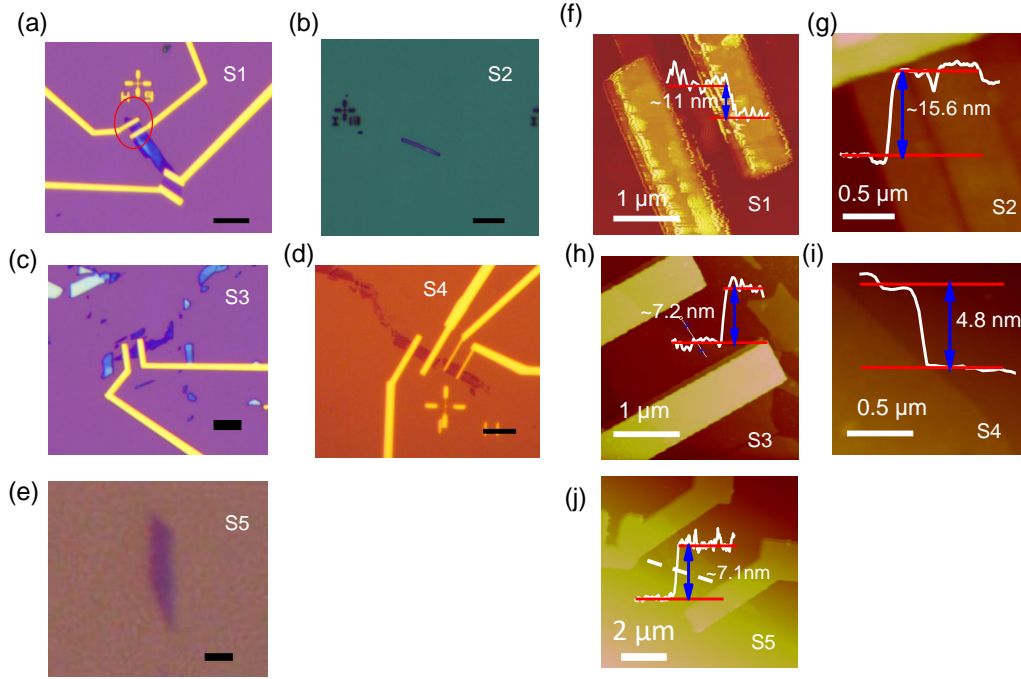


Fig. S1: Optical image of different $1T'$ - MoTe_2 nanocrystals with varying thickness (a) Sample S1, with thickness ~ 11 nm. (b) Sample S2, with thickness ~ 16 nm. (c) Sample S3, with thickness ~ 7 nm, and (d) Sample S4, with thickness ~ 5 nm. (e) (d) Sample S5, with thickness ~ 7 nm. (f)-(i) AFM image of S1, S2, S3, S4 and S5. Inset shows their height profile.

* These authors contributed equally

[†] anindya@iisc.ac.in

[‡] asood@iisc.ac.in

II. ADDITIONAL TRANSPORT DATA

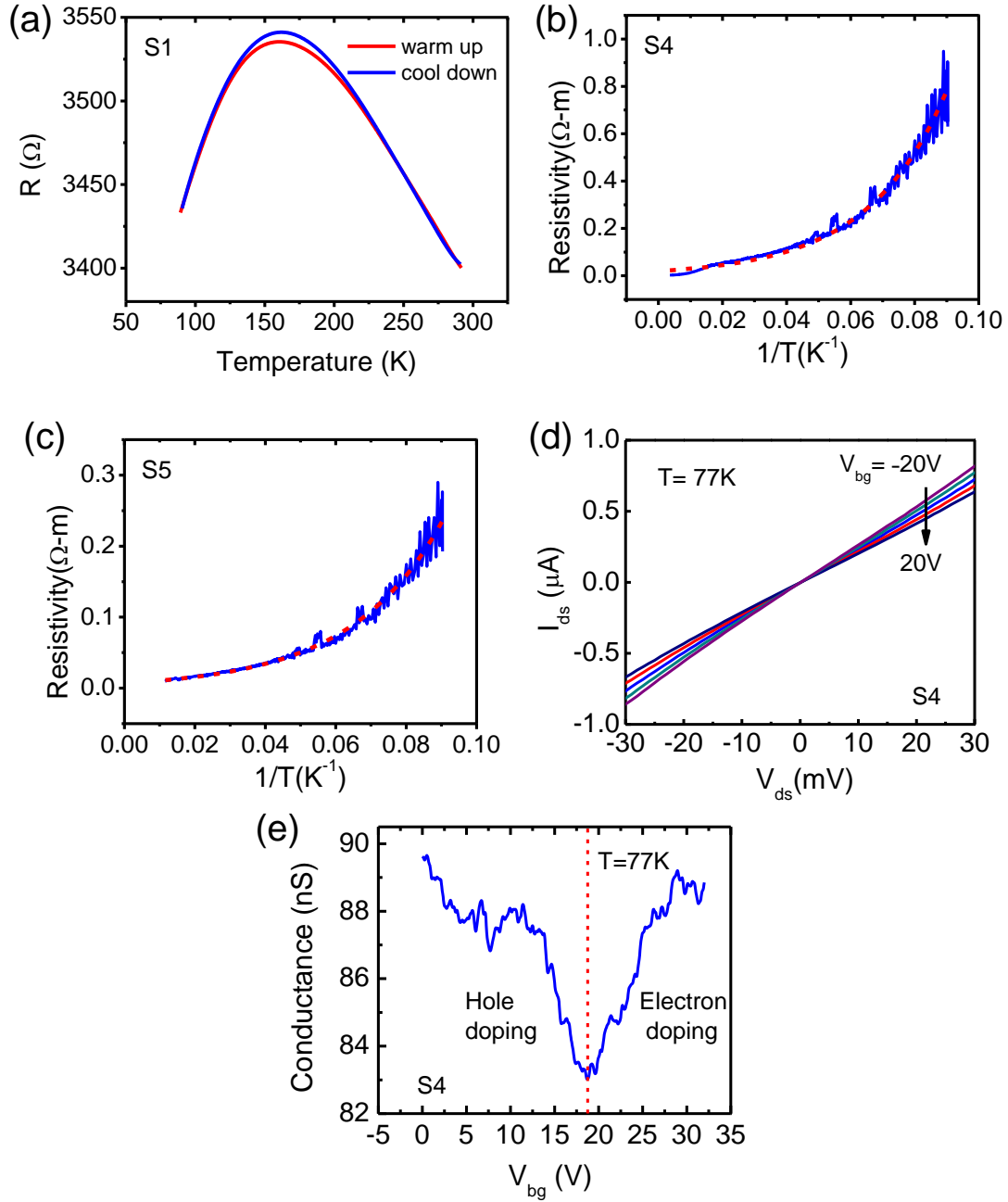


Fig. S2: (a) Resistance versus temperature plot for warming up and cooling down for 11nm nanocrystal. Resistivity versus temperature data (blue line) fit with Arrhenius equation (red dotted line) for (b) 5nm and (c) 7nm nanocrystals respectively. (d) Drain current (I_{ds}) with drain voltage (V_{ds}) plot for five different gate voltages of 5nm nanocrystal at 77K temperature. (e) Conductance of 5nm device plot with back gate voltage (V_{bg}) at 77K. Dotted red line indicates V_{bg} for minimum conductance separating electron and hole dominated drain current.

III. ADDITIONAL RAMAN DATA

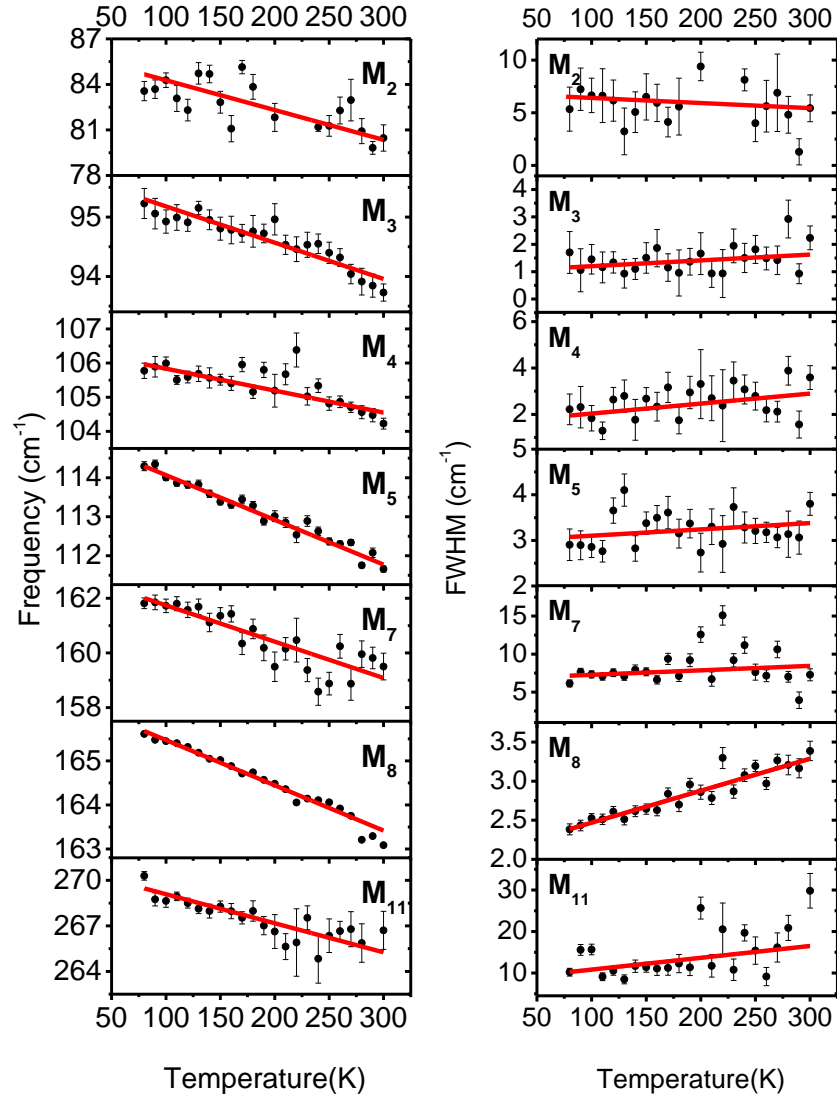


Fig. S3: Variation of (a) Frequency and (b) FWHM with temperature of M_2 , M_3 , M_4 , M_5 , M_7 , M_8 and M_{11} mode. Red lines shows their respective cubic anharmonic fitting.

TABLE S1: Calculated value of the cubic anharmonic coefficients and electron-phonon coupling term

Coefficients (cm^{-1})	M_1	M_6	M_9	M_{10}
A	0	0.4 ± 0.1	1.1 ± 0.8	3.5 ± 0.8
B	0	1.1 ± 0.7	1.5 ± 0.6	12.0 ± 4.5
C	1.07 ± 0.4	0	5.1 ± 1.7	3.5 ± 1.3
D	4.1 ± 1.3	3.9 ± 1.2	6.9 ± 1.9	27.0 ± 7.9